Chemical processing of sulfur dioxide enhances cloud sensitivity to aerosols

Matthew W. Christensen[1*], Andrew Gettelman[1], Laura Fierce[1], Manish Shrivastava[1], Coty Jen[2], Rahul A. Zaveri[1], Duncan Watson-Parris[3], and Philip Stier[4]

[1]Pacific Northwest National Laboratory, Richland, WA, USA
[2]Carnegie Mellon University, Pittsburgh, PA, USA
[3]Scripps Institution of Oceanography and Halıçoğlu Data Science Institute, University of California San Diego, USA
[4]Atmospheric, Oceanic and Planetary Physics, Department of Physics, University of Oxford, Oxford OX1 3PU, UK
[*]Correspondence: Matt.Christensen@pnnl.gov

August 25, 2026

Interactions between aerosols and clouds represent a major source of uncertainty in our understanding of the planetary energy balance. Increased aerosol concentrations can produce more numerous, smaller cloud droplets, enhancing the reflection of clouds and offsetting greenhouse gas warming. Gas-phase oxidation of sulfur dioxide plays a crucial role in forming new aerosols, yet little is known about their evolution or relationship to cloud lifetime and radiative forcing. Here we track cloud properties within aerosol plumes from four remote volcanic islands and two industrial power plants in satellite observations and general circulation model simulations. The simulated cloud perturbations agree, within uncertainty, with those derived from several hundred hand-logged and thousands of modeled pollution tracks in satellite imagery. Gas-to-particle conversion of sulfur dioxide in pollution tracks enhances concentrations of cloud condensation nuclei and cloud droplets, prolonging cloud brightening and increasing cloud albedo by 29% compared to simulations without this chemical processing. Particle-resolved aerosol box model calculations support these results and suggest that coagulation of newly formed particles is the dominant mechanism by which they grow to sizes relevant for cloud condensation nuclei. These findings suggest that as anthropogenic emissions decline, clouds influenced by sulfur dioxide will become dimmer, possibly accelerating global warming.

Aerosols can significantly cool the Earth by increasing cloud albedo and coverage. However, the magnitude of this radiative cooling is highly uncertain[1], partly because aerosol and cloud life cycles remain poorly understood. Aerosol plume lifetime is difficult to characterize and depends on dispersion, photolysis, and gas-to-particle conversion[2], while aerosol effects on cloud lifetime are similarly complex. Natural experiments[3] involving volcanic, shipping, and industrial emissions can produce long reflective cloud lines, known as "pollution tracks," and offer insights into the effects of sudden SO_2 increases on aerosol properties and cloud evolution. Generally, the emitted aerosols mix rapidly into planetary boundary layer (PBL) clouds, increasing cloud droplet number concentration (N_d), reducing droplet size, and enhancing cloud albedo[4]; this is known as the Twomey effect. However, introduced aerosol can suppress precipitation and hasten cloud-top entrainment over hours to days. These processes may increase or decrease liquid water path (LWP) and cloud fraction, depending on meteorological conditions[3], adding substantial uncertainty to the cloud albedo effect. The influence of chemical processing on cloud radiative effects and longevity remains largely unstudied in natural experiments.

Large eddy simulation (LES) experiments have been essential for quantifying cloud lifetime changes from aerosol plume perturbations but often lack complex chemistry[5,6]. Much of this investigation has occurred at regional scales using dispersion aerosol-box models[2], focusing on cloud-free conditions from limited case studies[4]. von Glasow et al.[2] estimated a 2-day chemical lifetime for shipping plumes (plume–background differences <5%), with elevated NO_x enhancing O_3 and OH production and accelerating SO_2 oxidation. Lack et al.[7] observed particle coagulation within ship plumes on similar timescales, shifting the aerosol size distribution toward larger particles. However, none of these studies connect chemical processing to the radiative effect of aerosol-cloud interactions (RE_{aci}), creating a crucial knowledge gap. Despite decades of progress, large uncertainties remain in the chemical pathways linking emissions to RE_{aci} (Fig. 1). By utilizing hundreds of observed pollution tracks and complementary atmosphere models, we identify the key chemical mechanisms that drive RE_{aci} across different natural experiments.

We quantify the impact of SO_2 chemical processing on RE_{aci} from four passively degassing volcanoes (Kīlauea, Ambrym, Yasur, Mt. Michael) and two industrial plants (Come By Chance Oil Refinery and Norilsk Nickel refinery). These locations were selected for their continuous, relatively large point-source emissions during 2015–2017, wide range of SO_2 emission rates, and relative isolation from other major aerosol sources (Extended Data Fig. 1; Extended Data Table 1). Aerosol evolution and gas-phase chemistry are modeled in version 6 of the Community Atmosphere Model (CAM6) General Circulation Model (GCM) and in offline calculations using the Particle Monte Carlo (PartMC) Model for Simulating Aerosol Interactions and Chemistry (MOSAIC) aerosol box model[8] (Methods). Simulated cloud perturbations are evaluated against several hundred pollution tracks identified in the MODerate Resolution Imaging Spectroradiometer (MODIS) satellite retrievals[9]. The Hybrid Single-Particle Lagrangian Integrated Trajectory (HYSPLIT) concentration plume model is used to simulate plumes and connect their effluents

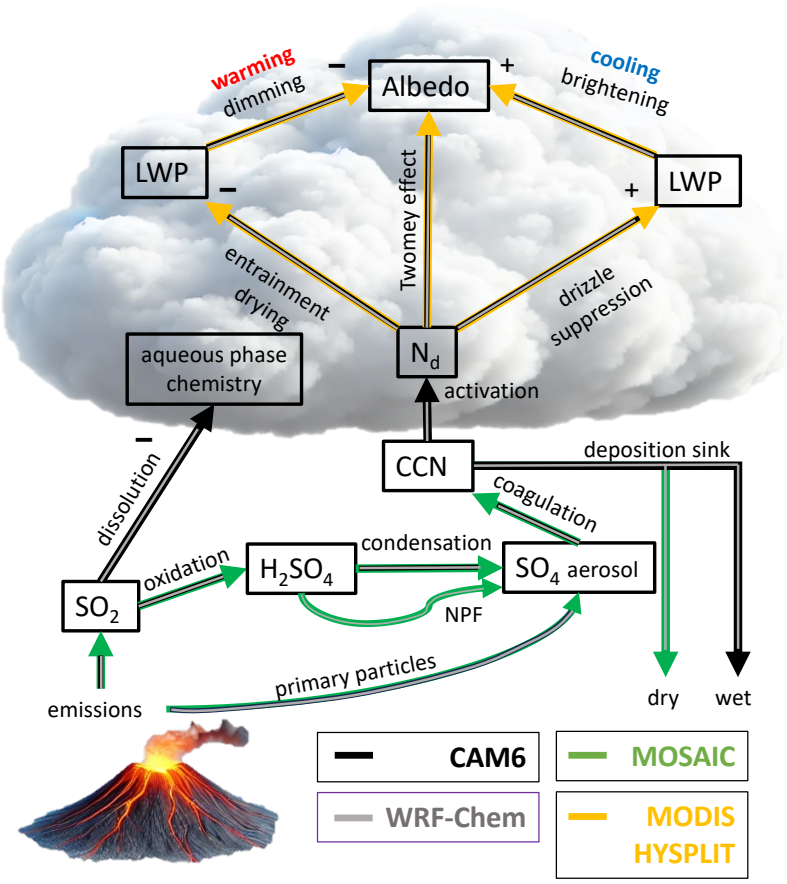


Fig. 1: Process chain from SO_2 emissions to cloud brightening. SO_2 is oxidized to H_2SO_4, which can nucleate new particles, condense into sulfate (SO_4), and grow to CCN via coagulation; removal occurs by aqueous dissolution and dry/wet deposition. CCN activation increases droplet number (N_d), affecting cloud albedo via the Twomey effect and LWP via drizzle suppression and entrainment. Tools constraining each step: CAM6 (black; GCM chemistry/microphysics), WRF-Chem (gray; high-resolution coupled meteorology–chemistry), PartMC–MOSAIC (green; particle-resolved NPF/condensation/coagulation), and HYSPLIT/MODIS (yellow; plume location/age and observed cloud perturbations).

to the clouds retrieved in satellite imagery. This step is necessary because cloud perturbations are often "invisible"[10] or not apparent through visual inspection especially far from the source. Here, HYSPLIT simulates plume dispersion, allowing perturbed clouds to be identified well beyond the typical lengths (~300 km) of most pollution tracks[4].

Long-Lasting Cloud Perturbation

Our method analyzes pollution tracks using visual identification and dispersion-based HYSPLIT modeling. Fig. 2 shows a pollution track downwind from the Come By Chance oil refinery in Newfoundland. An evident increase in N_d is notable (Fig. 2a). A series of positions outlining its shape is hand logged by visual inspection of the 2.1 μm near infrared reflectance ($R_{2.1\mu m}$) MODIS image (blue connected dots in Fig. 2b). Next,

we apply the Semi-Automated Polluted Cloud Detection Scheme (SAPCDS; Methods) to satellite imagery containing the hand-logged track locations (Fig. 2c) and extract polluted clouds along the pollution track. SAPCDS aggregates pixels along the track into 30-km segments and classifies them as polluted where the $R_{2.1\mu m}$ is significantly elevated[11]. Polluted clouds are also identified independently using the HYSPLIT dispersion model. Instead of a single parcel trajectory with an assumed constant width as used previously[10], HYSPLIT simulates plume width, which can be compared directly to hand-logged tracks using SAPCDS. The two methods broadly agree, with similar plume widths and positions in this case (Fig. 2d). In both methods, N_d is significantly higher in polluted clouds compared to unpolluted clouds (red vs blue lines) and remains perturbed for up to 500 km (Fig. 2e). Beyond this distance, the perturbation is indistinguishable.

At each site, we manually log distinct pollution tracks in MODIS imagery. Extended Data Table 1 summarizes the number of tracks identified during 2015–2017. Tracks are most frequent at Mt. Michael (38% occurrence) despite its relatively low SO_2 emissions (Extended Data Fig.1). Track occurrence at these sites also exceeds global ship-track estimates[12], likely from more favorable meteorological conditions with abundant low-level cloud[13], larger emissions than individual ships, and more exhaustive inspection. Although the island wake effect can occasionally cause leeward convergence, enhancing cloud brightness and complicating attribution to aerosol effects, the impact is generally distinguishable from nearby non-volcanic islands[14] (Supplementary Fig. 1). Our hand-logged tracks also provide a unique opportunity to validate HYSPLIT skill in simulating particle dispersion.

On average, both traditional hand-logged approaches and HYSPLIT-derived plumes show strong increases in N_d across all sites (Fig. 3a,b). If HYSPLIT perfectly matched the location and width of hand-logged tracks, the results would be identical to SAPCDS. However, errors in wind velocity and dispersion can cause the HYSPLIT-modeled plume to be slightly offset from the actual track location (Extended Data Figs. 2 and 3.; Supplementary Fig. 2). Due to these errors, HYSPLIT underestimates the N_d perturbation by about 30% on average, similar to using a single parcel trajectory approach to identify invisible ship tracks[10]. Averaged across all sites, N_d decreases rapidly within the first 300 km but remains significantly perturbed out to 1,000 km (roughly 24 hours from the source) (Fig. 3 and Extended Data Fig. 4). HYSPLIT predicts longer-lived cloud perturbations, yielding about three times more segment samples but with smaller perturbations than the manually logged SAPCDS tracks.

By contrast, LWP responses vary substantially across sites (Extended Data Fig. 4). At Kīlauea, elevated N_d perturbations broadly match the multi-site mean, but both polluted and unpolluted clouds show downstream decreases in N_d and LWP, likely reflecting island-wake flow and enhanced entrainment drying[14] there. More generally, background LWP gradients may reflect meteorological variability or artificial signals identified in HYSPLIT-based virtual ship-track studies[15,16], where correlated winds and cloud fields can produce spurious LWP anomalies[16]. Because the aggregate HYSPLIT-based LWP response is small and statistically indistinguishable from zero ($\Delta \ln(\mathrm{LWP}) = -0.02 \pm 0.10$; Extended Data

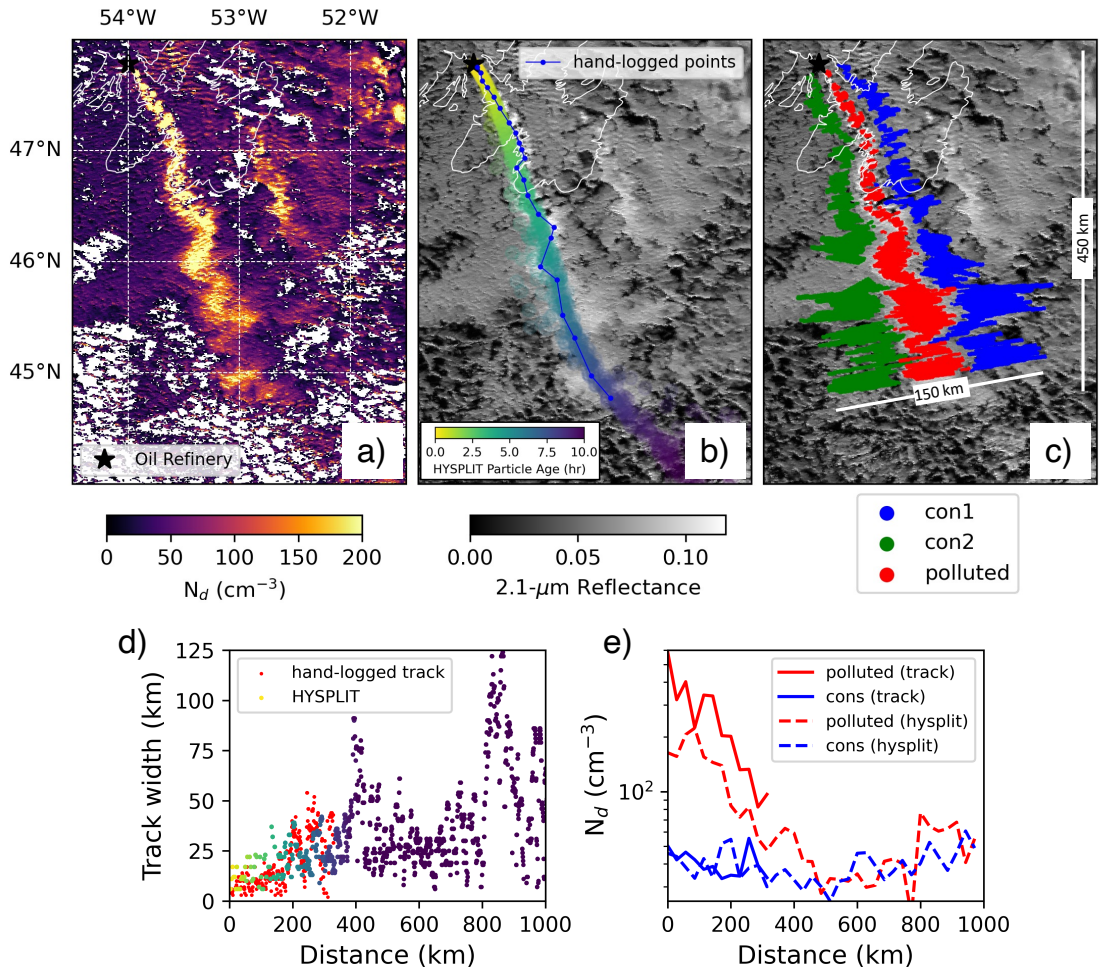


Fig. 2: Pollution track detection in satellite imagery. Cloud droplet number concentration (N_d) retrieved from MODIS near Come By Chance oil refinery, Newfoundland, on 25 November 2016, 16:40 UTC (a). Hand-logged track positions (blue connected dots) and HYSPLIT-simulated particle distribution (color scaled by age; yellow-to-purple) using HYSPLIT overlaid on the 2.1 µm near-infrared reflectance image (b). Polluted (red) and unpolluted segments (con1; blue and con2; green) clouds identified using SAPCDS are displayed with distance-scales overlaid (c). Track width along the plume is computed from hand-logged positions (red dots) and HYSPLIT (yellow-to-purple dots scaled by age) (d). N_d averaged as a function of distance from the refinery for polluted (red) and unpolluted clouds (mean of con1 and con2; blue), using hand-logged track positions (solid lines) and HYSPLIT positions (dashed lines) (e).

Table 2), we interpret it cautiously, consistent with weak mean LWP responses reported by Toll et al. (2019)[17].

From gas-phase chemistry to aerosol-cloud interactions

The CAM6 model is used to determine whether the long-lasting cloud perturbations observed by satellite are influenced by gas-phase chemistry. SO_2 emissions are connected to the Modal Aerosol Module (MAM4) which represents the evolution of the aerosol size

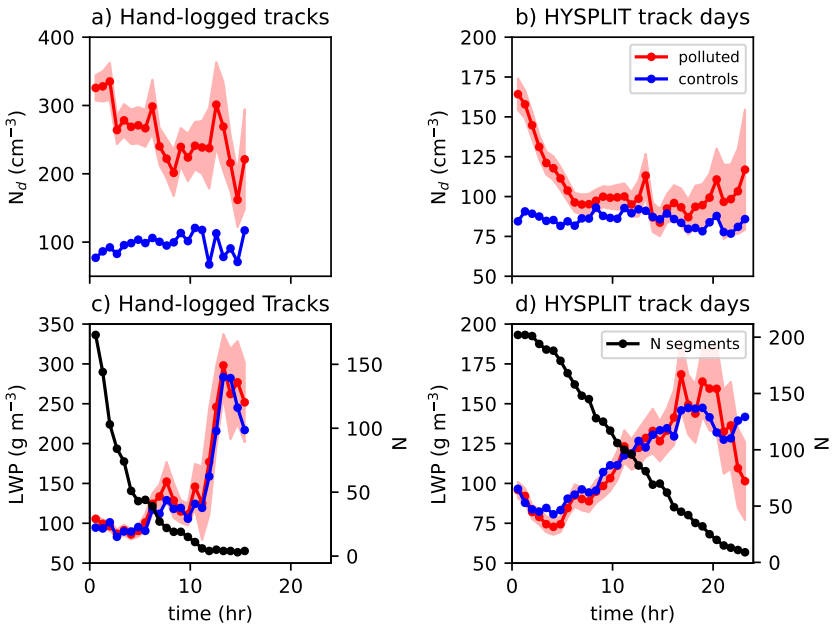


Fig. 3: Observed downstream cloud responses in pollution tracks. Average cloud droplet number concentration (N_d) (a,b) and liquid water path (LWP) (c,d) for polluted (red) and unpolluted (blue) MODIS cloud retrievals from hand-logged tracks (a,c) and those extracted from HYSPLIT plumes (b,d), plotted against distance from the aerosol source across all sites during 2015–2017. The number of segments (N) is shown for hand-logged tracks (c) and HYSPLIT plumes (d); error envelopes for polluted clouds represent the standard error about the mean.

distribution. The fraction of SO_2 emissions assumed to be primary sulfate aerosol is 2.5%, and SO_2 oxidation and aqueous scavenging are based on fixed oxidants (Methods). Fig. 4 shows three simulation experiments at Kīlauea: 1) **baseline** uses 2010 background emissions with no volcanic additions, 2) **baseline+plume** adds both SO_4 and SO_2 volcanic emissions, and 3) **plume-noSO$_2$** adds only SO_4 volcanic emissions. Emissions are tracked in a Lagrangian framework, with CAM6 trajectories computed from the 3D winds, initialized at the vent height, updated hourly over 24 hours, and plume edges defined by SO_2 percentile thresholds along the plume (Extended Data Fig. 5).

In the Kīlauea plume experiments, SO_2 concentrations peak near the vent and gradually decrease downstream in the **baseline+plume** run (Fig. 4a). Sulfate concentrations are initially high near the vent, increase slightly over time, and then decrease. CCN concentrations are also high at the vent and, rather than diminishing through dilution, they actually increases over time. This increase occurs only when SO_2 emissions are combined with primary SO_4 emissions (comparing the red and gray lines in Fig. 4c). Adding SO_2 gas to the aerosol plume (**baseline+plume**; red line) nearly doubles the CCN concentration (at 0.1% supersaturation) and sustains it longer than the **plume-noSO$_2$** run (gray line). The downstream increase in CCN is primarily due to SO_2 chemical processing in the aerosol plume rather than meteorological factors, as responses are consistent across experiments (Extended Data Fig. 6). As in the satellite analysis, N_d is high near the vent and remains elevated for more than 12 hours, although the responses in the hand-

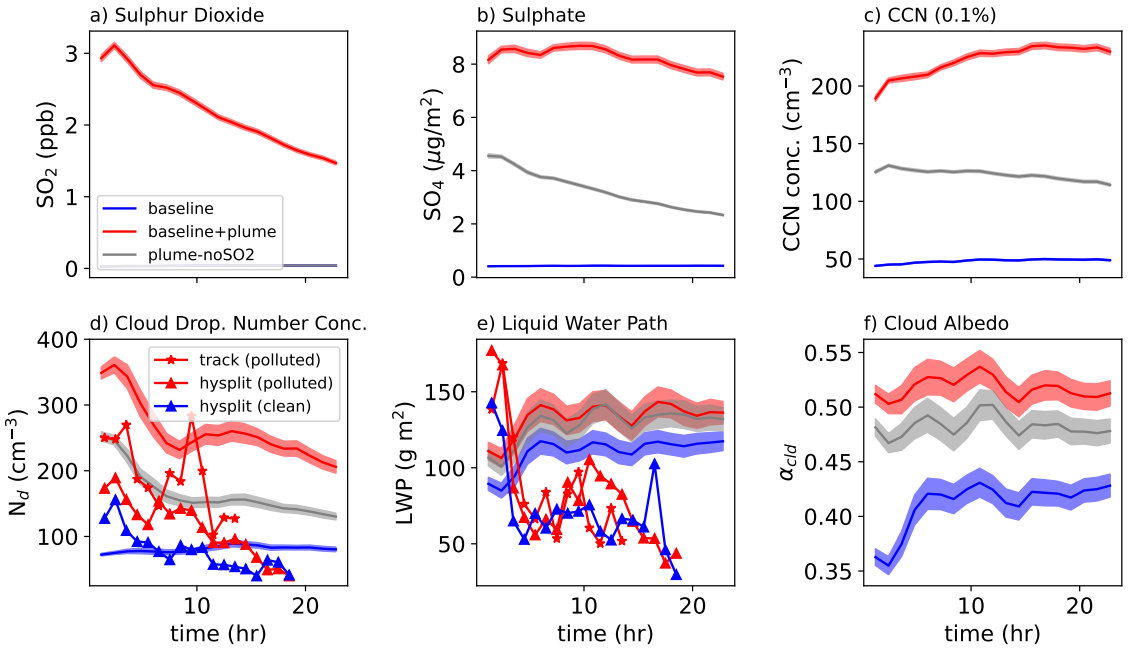


Fig. 4: CAM6 simulated responses of gas, aerosol, and cloud downstream from Kīlauea. Concentrations of sulfur dioxide (a), sulfate (b), cloud condensation nuclei (c), cloud droplet number concentration (N_d) (d), liquid water path (LWP) (e), and cloud albedo (f), shown as a function of time downstream from the vent and interpolated to the vent height of 1,247 m above sea level and averaged each day over the 2015–2017 period. The baseline run is represented in blue, the baseline run with the plume added in red, and the plume without SO_2 added in gray. Averages and error envelopes, represented by the full standard deviation from 1095 sample days, are displayed. Satellite-retrieved N_d is shown for polluted (red triangle) and unpolluted (blue triangle) clouds from HYSPLIT as well as from SAPCDS track positions (red; *).

logged and HYSPLIT simulated tracks are less pronounced than in CAM6 (Fig. 4d). This may indicate that aerosol sources in CAM6 are too strong or that the aerosol plume does not dilute quickly enough at Kīlauea, likely because of the GCM's coarse grid resolution (Supplementary Methods 1.1).

To better understand the processes driving increased CCN concentrations over time, we run the stochastic, particle-resolved PartMC-MOSAIC aerosol box model (Methods). Fig. 5 shows PartMC-MOSAIC simulations of Kīlauea, initialized with an SO_2 concentration of 100 ppb, typically observed just above Halema'uma'u Crater vent[18]. Simulations use CAM6 meteorology for the trajectory shown in Extended Data Fig. 5. SO_2 declines over time because of dilution and gas-to-particle conversion of SO_4. CCN concentration at 0.1% supersaturation rises gradually over 24 hours (Fig. 5b). At 0.3%, the CCN concentration rises rapidly before 10 hours, then declines (Fig 5c). New particles form immediately, but if coagulation is turned off, they remain too small to be CCN-active. Semi-volatile material also condenses onto new and pre-existing particles, but the gradual CCN increase is driven by coagulation among the newly formed particles. Coagulation, rather than condensation,

is the dominant mechanism bringing particles to CCN-relevant sizes. The process chain is therefore: gas-phase chemistry drives new particle formation, followed by coagulation among the newly formed particles. Overall, with new particle formation and condensation, PartMC-MOSAIC shows that CCN concentrations do indeed increase downstream from the vent, similar to CAM6.

SO_2, SO_4, and CCN concentrations also evolve downwind across volcanoes ranging from the strongest-emitting (Ambrym) to the weakest-emitting (Mt. Michael) in CAM6 (Extended Data Fig. 7). At sites with the largest SO_2 emissions (i.e., Ambrym, Kīlauea, Yasur), CCN concentrations tend to increase away from the vent and maximize downstream. In contrast, at sites emitting less SO_2 (e.g., Mt. Michael), CCN tends to decrease downstream. This CAM6 result agrees with a series of PartMC-MOSAIC perturbation experiments in which the initial SO_2 concentration is increased (Extended Data Fig. 8). As SO_2 emissions decrease, downstream CCN dilution becomes more rapid than CCN production via NPF and coagulation. These simulations show that coagulation is largely responsible for the increasing CCN concentrations downstream over time.

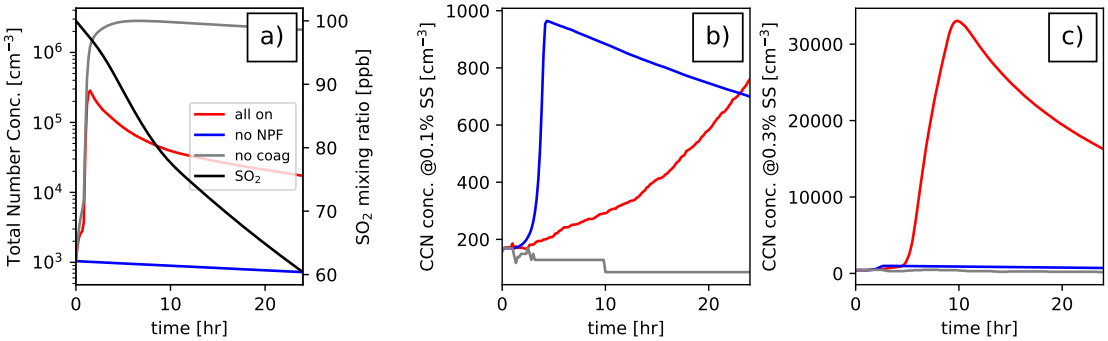


Fig. 5: PartMC-MOSAIC simulations of gas-phase chemistry and its effects on CCN. Total aerosol number concentration simulated over a 24-hour period based on CAM6 meteorological data at Kīlauea on 6/13/2015, overplotted with SO_2 mixing ratio for an initial 100 ppbv SO_2 puff-perturbation (a). CCN concentration at 0.1% (b) and 0.3% supersaturation (c) for simulations with no coagulation (green), no new particle formation (NPF; blue), and both coagulation and NPF enabled (red).

Chemical Processing of SO_2 Boosts CCN and Brightens Clouds

CAM6 simulates robust near-source increases in SO_2, SO_4, and CCN at each site (Fig. 6), with smaller changes at the Come By Chance oil refinery, where emissions are relatively weak and dilute rapidly. Cloud properties respond with decreases in droplet effective radius (R_e) and increases in cloud optical thickness (τ_c), LWP, and N_d, with the magnitude of these perturbations increasing even more when SO_2 is included in the emissions. Changes in low-level cloud fraction are negligible in CAM6, although satellite observations show small increases.

Satellite-based estimates provide an observational constraint on these responses. CAM6 cloud perturbations generally fall between the hand-logged and HYSPLIT means (stars

and triangles in Fig. 6b). These retrievals define an observational range: hand-logged tracks (using SAPCDS) yield stronger but more selective perturbations, whereas HYSPLIT yields weaker estimates from broader plume sampling that also captures invisible or diffuse plumes. CAM6 reproduces the observed sign and broad magnitude of the cloud responses within this range, increasing confidence in the modeled enhancement of CCN and cloud brightening from SO_2 processing. We use 4–10 h rather than 0–10 h to avoid near-source land contamination and to sample the plume after offshore advection; 4 h provides a consistent, site-independent window that captures the chemically enhanced CCN phase for model-satellite comparison.

The RE_{aci} (Methods) is decomposed into the Twomey effect, liquid water path adjustment (LWP_{adj}), and cloud fraction adjustment (CF_{adj}). Estimates of RE_{aci} are averaged across all locations and summarized in Extended Data Table 2. In CAM6, RE_{aci} is -9.9 ± 3.6 W m^{-2}, computed from the difference between the plume and baseline simulations. This value agrees reasonably well with satellite data, lying between the track-based and HYSPLIT-based estimates. LWP_{adj} contributes approximately 31% of the RE_{aci}, with the Twomey effect accounting for 69%, as CF_{adj} is negligible in CAM6. Although LWP_{adj} and CF_{adj} are larger in the satellite analysis, both remain statistically insignificant in the track- and HYSPLIT-based estimates according to a two-tailed t-test at the 95% confidence level. When SO_2 is turned off, RE_{aci} changes to -7.7 ± 4.3 W m^{-2}, decreasing its magnitude by 29 ± 8%. Over timescales of 12–24 hours, RE_{aci} decreases by 10% relative to 1–12 hours. These calculations point to the importance of chemical processing in elevating CCN concentrations and enhancing RE_{aci}.

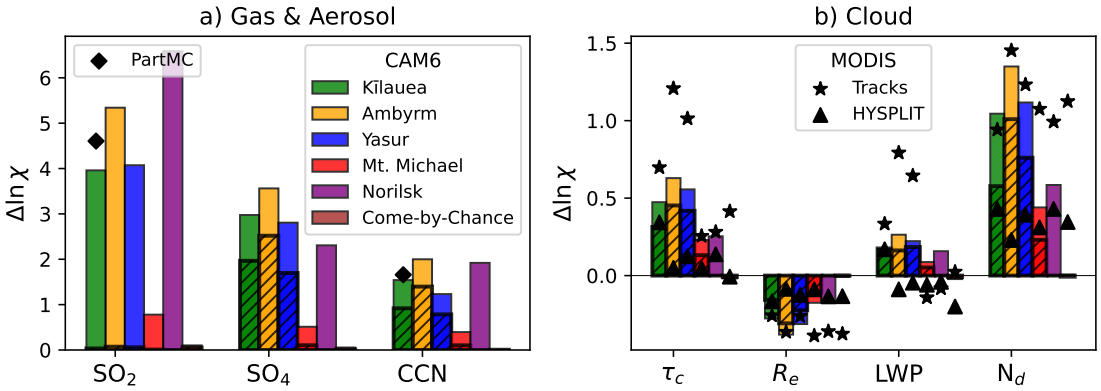


Fig. 6: Gas, aerosol, and cloud responses in natural experiments. Log differences in the variables (χ), sulfur dioxide (SO_2), sulfate (SO_4), and Cloud Condensation Nuclei (CCN) concentration at 0.1% supersaturation, between polluted (plume) and clean (baseline) CAM6 simulations averaged during the 4–10 hour interval along trajectories during 2015–2017 at each location, and for the PartMC experiments at Kīlauea (100 and 1.0 ppb; diamond) (a). Hatched bars represent the CAM6 **plume-noSO$_2$** experiment. Cloud optical thickness (τ_c), cloud droplet effective radius (R_e), liquid water path (LWP), and cloud droplet number concentration (N_d) are displayed alongside MODIS results for both the track (star) and HYSPLIT (triangle) segments.

Discussion & Conclusion

By combining satellite observations with modeling, we show how aerosol plume evolution influences CCN production and aerosol–cloud lifetime effects in natural experiments. Using multiple detection methods, including traditional hand-logged tracks and plume modeling, we show that strong perturbations persist for several hundred kilometers downstream of their emission sources, consistent with past research [4,17,3]. Our results further suggest that part of this enhanced cloud brightening arises from the chemical processing of SO_2, which prolongs and elevates CCN concentrations.

These results also help clarify how different plume-detection methods shape the inferred cloud response. HYSPLIT yields roughly three times as many samples as hand-logging and captures clouds that may not be visibly polluted, providing unique constraints for estimating RE_{aci}. However, errors in the driving winds can misplace the plume and dilute the polluted sample with clean pixels, producing weaker cloud-property perturbations in satellite observations. We therefore expect the mean cloud response, and the CAM6 all-day average, to lie between the stronger hand-logged SAPCDS track estimates, which represent selected days with favorable meteorology, and the weaker HYSPLIT-derived plume estimates, which include both visible and invisible tracks throughout the year. This interpretation is consistent with recent work on ship tracks [19], which suggests that using HYSPLIT to identify polluted clouds may substantially underestimate cloud perturbations. Furthermore, Yuan et al. (2025b) [20] found that machine-detectable ship tracks account for only a small fraction (5%) of the total radiative effect inferred from top-down statistical constraints over a shipping corridor, suggesting that traditional hand-logged tracks may represent an upper bound and HYSPLIT-derived tracks a lower bound.

In CAM6, clouds are significantly brighter when SO_2 gas is included with primary aerosol emissions. As in the satellite observations, N_d is strongly enhanced near the source. High CCN concentrations also persist for up to 24 hours, or roughly 1,000 km, downstream of volcanic emission sources. Including SO_2 in the plume enhances CCN growth over time through gas-phase oxidation of SO_2 and subsequent growth by coagulation. The reliability of our findings is further supported by PartMC-MOSAIC. Aerosol nucleation and growth involve computationally expensive parameterizations that are often absent in LES simulations of natural experiments [6]. Failing to represent aerosol evolution in high-resolution LES models may therefore shorten cloud lifetimes and confound interpretation of aerosol impacts on clouds in natural experiments [21]. Accounting for SO_2 oxidation, new particle formation, and coagulation-driven growth to CCN-relevant sizes increases the magnitude of RE_{aci} (i.e., makes the forcing more negative) by approximately 29% in CAM6. As global anthropogenic SO_2 emissions decline, boundary layer clouds may become dimmer, reflect less solar radiation to space, and possibly accelerate future global warming [22]. It is thus crucial to consider not only cloud sensitivity to aerosol-induced property changes but also the chemical processing linked to SO_2 emissions when assessing aerosol radiative forcing and future warming.

Acknowledgments

We thank the Aerosol, Cloud, Precipitation, and Climate (ACPC) initiative and its members for the engaging discussions that helped shape this research.

Funding

This research was partially supported by the Atmospheric System Research (ASR) program as part of the US Department of Energy, Office of Science, Office of Biological and Environmental Research under Pacific Northwest National Laboratory (PNNL) project 57131. PNNL is operated for the US Department of Energy by Battelle Memorial Institute under contract DE-A06-76RLO 1830. This research was partly supported by European Research Council Project constRaining the EffeCts of Aerosols on Precipitation under the European Union's Horizon 2020 Research and Innovation Program Grant 724602 and by the Atmospheric Composition and Radiative forcing changes due to UN International Ship Emissions regulations (ACRUISE) Natural Environment Research Council (NE/S005099/1).

Author contributions

M.W.C. carried out the analysis and wrote the paper, with contributions from all coauthors. A.G. provided the CAM6 data, L.F. provided the PartMC-MOSAIC data, M.S. provided the WRF-Chem model, C. J., R.Z., D.W.P., and P.S. provided feedback on the analysis and editing.

Correspondence and requests for materials

should be addressed to Matthew Christensen.

Competing Interests

The authors declare no competing interests.

Figure Legends/Captions (for main text figures)

Figure 1: **Process chain from SO_2 emissions to cloud brightening.** SO_2 is oxidized to H_2SO_4, which can nucleate new particles, condense into sulfate (SO_4), and grow to CCN via coagulation; removal occurs by aqueous dissolution and dry/wet deposition. CCN activation increases droplet number (N_d), affecting cloud albedo via the Twomey effect and LWP via drizzle suppression and entrainment. Tools constraining each step: CAM6

(black; GCM chemistry/microphysics), WRF-Chem (gray; high-resolution coupled meteorology–chemistry), PartMC–MOSAIC (green; particle-resolved NPF/condensation/coagulation), and HYSPLIT/MODIS (yellow; plume location/age and observed cloud perturbations).

Figure 2: **Pollution track detection in satellite imagery.** Cloud droplet number concentration (N_d) retrieved from MODIS near Come By Chance oil refinery, Newfoundland, on 25 November 2016, 16:40 UTC (a). Hand-logged track positions (blue connected dots) and HYSPLIT-simulated particle distribution (color scaled by age; yellow-to-purple) using HYSPLIT overlaid on the 2.1 µm near-infrared reflectance image (b). Polluted (red) and unpolluted segments (con1; blue and con2; green) clouds identified using SAPCDS are displayed with distance-scales overlaid (c). Track width along the plume is computed from hand-logged positions (red dots) and HYSPLIT (yellow-to-purple dots scaled by age) (d). N_d averaged as a function of distance from the refinery for polluted (red) and unpolluted clouds (mean of con1 and con2; blue), using hand-logged track positions (solid lines) and HYSPLIT positions (dashed lines) (e).

Figure 3: **Observed downstream cloud responses in pollution tracks.** Average cloud droplet number concentration (N_d) (a,b) and liquid water path (LWP) (c,d) for polluted (red) and unpolluted (blue) MODIS cloud retrievals from hand-logged tracks (a,c) and those extracted from HYSPLIT plumes (b,d), plotted against distance from the aerosol source across all sites during 2015–2017. The number of segments (N) is shown for hand-logged tracks (c) and HYSPLIT plumes (d); error envelopes for polluted clouds represent the standard error about the mean.

Figure 4: **CAM6 simulated responses of gas, aerosol, and cloud downstream from Kīlauea.** Concentrations of sulfur dioxide (a), sulfate (b), cloud condensation nuclei (c), cloud droplet number concentration (N_d) (d), liquid water path (LWP) (e), and cloud albedo (f), shown as a function of time downstream from the vent and interpolated to the vent height of 1,247 m above sea level and averaged each day over the 2015–2017 period. The baseline run is represented in blue, the baseline run with the plume added in red, and the plume without SO_2 added in gray. Averages and error envelopes, represented by the full standard deviation from 1095 sample days, are displayed. Satellite-retrieved N_d is shown for polluted (red triangle) and unpolluted (blue triangle) clouds from HYSPLIT as well as from SAPCDS track positions (red; *).

Figure 5: **PartMC-MOSAIC simulations of gas-phase chemistry and its effects on CCN.** Total aerosol number concentration simulated over a 24-hour period based on CAM6 meteorological data at Kīlauea on 6/13/2015, overplotted with SO_2 mixing ratio for an initial 100 ppbv SO_2 puff-perturbation (a). CCN concentration at 0.1% (b) and 0.3% supersaturation (c) for simulations with no coagulation (green), no new particle formation (NPF; blue), and both coagulation and NPF enabled (red).

Figure 6: **Gas, aerosol, and cloud responses in natural experiments.** Log differences in the variables (χ), sulfur dioxide (SO_2), sulfate (SO_4), and Cloud Condensation Nuclei (CCN) concentration at 0.1% supersaturation, between polluted (plume) and clean (baseline) CAM6 simulations averaged during the 4–10 hour interval along trajectories

during 2015–2017 at each location, and for the PartMC experiments at Kīlauea (100 and 1.0 ppb; diamond) (a). Hatched bars represent the CAM6 **plume-noSO_2** experiment. Cloud optical thickness (τ_c), cloud droplet effective radius (R_e), liquid water path (LWP), and cloud droplet number concentration (N_d) are displayed alongside MODIS results for both the track (star) and HYSPLIT (triangle) segments.

References

[1] N. Bellouin, J. Quaas, E. Gryspeerdt, S. Kinne, P. Stier, D. Watson-Parris, O. Boucher, K. S. Carslaw, M. Christensen, A.-L. Daniau, J.-L. Dufresne, G. Feingold, S. Fiedler, P. Forster, A. Gettelman, J. M. Haywood, U. Lohmann, F. Malavelle, T. Mauritsen, D. T. McCoy, G. Myhre, J. Mulmenstadt, D. Neubauer, A. Possner, M. Rugenstein, Y. Sato, M. Schulz, S. E. Schwartz, O. Sourdeval, T. Storelvmo, V. Toll, D. Winker, and B. Stevens. Bounding global aerosol radiative forcing of climate change. *Reviews of Geophysics*, 58(1):e2019RG000660, 2020. doi: 10.1029/2019RG000660. URL `https://agupubs.onlinelibrary.wiley.com/doi/abs/10.1029/2019RG000660`. e2019RG000660 10.1029/2019RG000660.

[2] R. von Glasow, M. G. Lawrence, R. Sander, and P. J. Crutzen. Modeling the chemical effects of ship exhaust in the cloud-free marine boundary layer. *Atmospheric Chemistry and Physics*, 3(1):233–250, 2003. doi: 10.5194/acp-3-233-2003. URL `https://acp.copernicus.org/articles/3/233/2003/`.

[3] M. W. Christensen, A. Gettelman, J. Cermak, G. Dagan, M. Diamond, A. Douglas, G. Feingold, F. Glassmeier, T. Goren, D. P. Grosvenor, E. Gryspeerdt, R. Kahn, Z. Li, P.-L. Ma, F. Malavelle, I. L. McCoy, D. T. McCoy, G. McFarquhar, J. Mülmenstädt, S. Pal, A. Possner, A. Povey, J. Quaas, D. Rosenfeld, A. Schmidt, R. Schrödner, A. Sorooshian, P. Stier, V. Toll, D. Watson-Parris, R. Wood, M. Yang, and T. Yuan. Opportunistic experiments to constrain aerosol effective radiative forcing. *Atmospheric Chemistry and Physics*, 22(1):641–674, 2022. doi: 10.5194/acp-22-641-2022. URL `https://acp.copernicus.org/articles/22/641/2022/`.

[4] P. A. Durkee, R. E. Chartier, A. Brown, E. J. Trehubenko, S. D. Rogerson, C. Skupniewicz, and K. E. Nielsen. Composite ship track characteristics. *Journal of the Atmospheric Sciences*, 57:2542–2553, 2000.

[5] H. Wang and G. Feingold. Modeling mesoscale cellular structures and drizzle in marine stratocumulus. part ii: The microphysics and dynamics of the boundary region between open and closed cells. *Journal of the Atmospheric Sciences*, 66:3257–3275, 2009. doi:10.1175/2009JAS3120.1.

[6] K. G. Pressel, T. Heus, Y. Zhang, C. van Heerwaarden, A. Jaruga, G. Matheou, M. Witte, L. Fierce, K. Lundquist, V. Ghate, F. Yang, C. Chiu, and D. Richter. Department of energy's atmospheric system research (asr) program's workshop on the future of atmospheric large eddy simulation (les): Workshop report. *USDOE Office of Science, Biological and Environmental Research*, 9 2023. doi: 10.2172/2004980. URL `https://www.osti.gov/biblio/2004980`.

[7] D. A. Lack, J. J. Corbett, T. Onasch, B. Lerner, P. Massoli, P. K. Quinn, T. S. Bates, D. S. Covert, D. Coffman, B. Sierau, S. Herndon, J. Allan, T. Baynard, E. Lovejoy,

A. R. Ravishankara, and E. Williams. Particulate emissions from commercial shipping: Chemical, physical, and optical properties. *Journal of Geophysical Research: Atmospheres*, 114(D7), 2009. doi: https://doi.org/10.1029/2008JD011300. URL https://agupubs.onlinelibrary.wiley.com/doi/abs/10.1029/2008JD011300.

[8] R. A. Zaveri, R. C. Easter, J. D. Fast, and L. K. Peters. Model for simulating aerosol interactions and chemistry (mosaic). *Journal of Geophysical Research: Atmospheres*, 113(D13), 2008. doi: https://doi.org/10.1029/2007JD008782. URL https://agupubs.onlinelibrary.wiley.com/doi/abs/10.1029/2007JD008782.

[9] S. Platnick, K. G. Meyer, M. D. King, G. Wind, N. Amarasinghe, B. Marchant, G. T. Arnold, Z. Zhang, P. A. Hubanks, R. E. Holz, P. Yang, W. L. Ridgway, and J. Riedi. The modis cloud optical and microphysical products: Collection 6 updates and examples from terra and aqua. *IEEE Transactions on Geoscience and Remote Sensing*, 55(1):502–525, 2017. doi: 10.1109/TGRS.2016.2610522.

[10] P. Manshausen, D. Watson-Parris, M. W. Christensen, J. P. Jalkanen, and P. Stier. Invisible ship tracks show large cloud sensitivity to aerosol. *Nature*, 610(7930):101–+, 2022. ISSN 0028-0836. doi: 10.1038/s41586-022-05122-0. URL <GotoISI>://WOS:000864365700023.

[11] M. W. Christensen and G. L. Stephens. Microphysical and macrophysical responses of marine stratocumulus polluted by underlying ships: Evidence of cloud deepening. *Journal of Geophysical Research: Atmospheres*, 116(D3), 2011. doi: 10.1029/2010JD014638.

[12] D. Watson-Parris, M. W. Christensen, A. Laurenson, D. Clewley, E. Gryspeerdt, and P. Stier. Shipping regulations lead to large reduction in cloud perturbations. *Proc Natl Acad Sci U S A*, 119(41):e2206885119, 2022. ISSN 1091-6490 (Electronic) 0027-8424 (Print) 0027-8424 (Linking). doi: 10.1073/pnas.2206885119. URL https://www.ncbi.nlm.nih.gov/pubmed/36191195. Watson-Parris, Duncan Christensen, Matthew W Laurenson, Angus Clewley, Daniel Gryspeerdt, Edward Stier, Philip eng Research Support, Non-U.S. Gov't 2022/10/04 Proc Natl Acad Sci U S A. 2022 Oct 11;119(41):e2206885119. doi: 10.1073/pnas.2206885119. Epub 2022 Oct 3.

[13] Coakley J. A. Jr., P. A. Durkee, K. Nielsen, J. P. Taylor, S. Platnick, B. A. Albrecht, D. Babb, F. L. Chang, W. R. Tahnk, C. S. Bretherton, and P. V. Hobbs. The appearance and disappearance of ship tracks on large spatial scales. *Journal of the Atmospheric Sciences*, 57:2765–2778, 2000.

[14] A. Schmidt, K. S. Carslaw, G. W. Mann, A. Rap, K. J. Pringle, D. V. Spracklen, M. Wilson, and P. M. Forster. Importance of tropospheric volcanic aerosol for indirect radiative forcing of climate. *Atmospheric Chemistry and Physics*, 12(16):7321–7339, 2012. doi: 10.5194/acp-12-7321-2012. URL https://acp.copernicus.org/articles/12/7321/2012/.

[15] P. Manshausen, D. Watson-Parris, M. W. Christensen, J.-P. Jalkanen, and P. Stier. Rapid saturation of cloud water adjustments to shipping emissions. *Atmospheric Chemistry and Physics*, 23(19):12545–12555, 2023. doi: 10.5194/acp-23-12545-2023. URL https://acp.copernicus.org/articles/23/12545/2023/.

[16] A. Tippett, E. Gryspeerdt, P. Manshausen, P. Stier, and T. W. P. Smith. Weak liquid water path response in ship tracks. *Atmospheric Chemistry and Physics*, 24(23):13269–13283, 2024. doi: 10.5194/acp-24-13269-2024. URL https://acp.copernicus.org/articles/24/13269/2024/.

[17] V. Toll, M. Christensen, J. Quaas, and N. Bellouin. Weak average liquid-cloud-water response to anthropogenic aerosols. *Nature*, 572:51–55, 2019. doi: https://doi.org/10.1038/s41586-019-1423-9.

[18] A. K. Pattantyus, S. Businger, and S. G. Howell. Review of sulfur dioxide to sulfate aerosol chemistry at kīlauea volcano, hawai'i. *Atmospheric Environment*, 185:262–271, 2018. ISSN 1352-2310. doi: https://doi.org/10.1016/j.atmosenv.2018.04.055. URL https://www.sciencedirect.com/science/article/pii/S1352231018302942.

[19] T. Yuan, H. Song, L. Oreopoulos, R. Wood, K. Meyer, A. Crawford, W. Smith, and R. Eastman. Analyses of virtual ship-tracks systematically underestimate aerosol-cloud interactions signals. *Geophysical Research Letters*, 52(7):e2024GL114356, 2025. doi: https://doi.org/10.1029/2024GL114356. URL https://agupubs.onlinelibrary.wiley.com/doi/abs/10.1029/2024GL114356. e2024GL114356 2024GL114356.

[20] T. Yuan, H. Song, L. F. Boss, and M. Diamond. Detectable ship tracks account for just 5% of aerosol indirect forcing from ship emissions. *Communications Earth & Environment*, 6(1):899, 2025. doi: 10.1038/s43247-025-02825-w. URL https://www.nature.com/articles/s43247-025-02825-w.

[21] F. Glassmeier, F. Hoffmann, J. S. Johnson, T. Yamaguchi, K. S. Carslaw, and G. Feingold. Aerosol-cloud-climate cooling overestimated by ship-track data. *Science*, 371(6528):485–+, 2021. ISSN 0036-8075. doi: 10.1126/science.abd3980. URL <GotoISI>://WOS:000612983100038.

[22] S. E. Bauer, K. Tsigaridis, G. Faluvegi, L. Nazarenko, R. L. Miller, M. Kelley, and G. Schmidt. The turning point of the aerosol era. *Journal of Advances in Modeling Earth Systems*, 14(12):e2022MS003070, 2022. doi: https://doi.org/10.1029/2022MS003070. URL https://agupubs.onlinelibrary.wiley.com/doi/abs/10.1029/2022MS003070. e2022MS003070 2022MS003070.

Methods

Volcanic activity All volcanic locations were relatively active during 2015–2017, according to version 2 of the global catalogue of large anthropogenic and volcanic SO_2 sources and emissions derived from satellite measurements[23]. Kīlauea was more active in 2008 than in 2007 (Extended Data Fig. 1). Ambrym volcanic activity declined substantially after 2018, whereas Yasur emissions increased from 2006–2022. Mt. Michael showed lower emissions in 2016 than in 2015 and 2017, possibly reducing the number of volcano tracks. Both industrial power plants operated throughout this period.

Satellite Observations The Aqua MODIS Collection 6.1 cloud product (MYD06_L2) is used to identify single-layer low-level cloud properties. Nadir retrievals have ∼1 km resolution, sufficient to resolve typical pollution track widths (∼ 7 km)[4]. Cloud optical thickness (τ_c) and effective droplet radius (R_e) are used to compute liquid water path ($LWP = 2/3\rho_l r_e \tau_c$, where ρ_l is the density of water) and cloud droplet number concentration ($N_d = \gamma\sqrt{\tau_c} r_e^{-2.5}$, where, $\gamma = 1.37e-5$ m$^{-0.5}$ is related to the adiabatic condensation growth rate and adiabaticity factor typical for stratocumulus clouds)[24]. Retrieval uncertainty increases for thin, broken, or inhomogeneous clouds. Grosvenor et al. (2018)[25] estimated ∼80 % uncertainty in N_d under ideal overcast conditions, whereas uncertainties in R_e and τ_c are typically <30%[25].

Semi-Automated Polluted Cloud Detection Scheme (SAPCDS) We use SAPCDS following Christensen and Stephens (2011)[11] to identify polluted and unpolluted pixels along pollution tracks. Tracks are logged by hand in the MODIS satellite imagery. Pixels are classified as polluted when the 2.1-μm near infrared reflectance exceeds a 3-standard deviation threshold within aggregated 30 × 50 km segments, a scale shown to be optimal given the 5–10 km auto-correlation scales typically found in the MODIS cloud optical property retrievals for PBL clouds[26]. After polluted pixels are identified (Fig. 2c), their distribution is symmetrically mapped onto both sides of the track to define the unpolluted control regions with equal sampling (green and blue pixels). Four adjacent pixels are removed at the polluted-cloud boundary to avoid contamination.

Plume Modeling using HYSPLIT Spatial particle distributions are simulated with HYSPLIT version 5 concentration plume model[27]. Emissions are treated as a single inert tracer released every 20 minutes for 24 hours before the Aqua satellite overpass. At each time step, 2,500 tracer particles are emitted from the source, tracked without chemistry or deposition, tagged by release time, and matched to the nearest 1-km MODIS pixel. Particle age, defined as the time since release, is used to characterize plume evolution along the trajectory. As in SAPCDS, plume pixels are placed symmetrically on both sides of the plume to form control pixels. Plume width is defined as the cross-plume distance spanning the 5th–95th percentile of particle positions, consistent with the CAM6 transect metric.

HYSPLIT is driven by the European Centre for Medium-Range Forecasts (ECMWF) ERA5 reanalysis data converted to Air Resources Laboratory (ARL) format. ERA5 has 31 km horizontal resolution (TL639 spectral grid) and 137 hybrid sigma pressure levels extending to 0.01 hPa (about 80 km altitude). Although HYSPLIT includes a simplified sulfur gas-to-particle conversion scheme, it represents only bulk sulfate with prescribed first-order rates and fixed deposition velocities, without aerosol size distributions, background SO_2, number concentrations, or CCN-relevant microphysics. We therefore, use it only for plume transport and dispersion.

Error Assessment of the Plume Model We assess the error in the plume model from three meteorological products, the Global Data Assimilation System (GDAS; $1^\circ \times 1^\circ$ spatial resolution), the National Centers for Environmental Prediction (NCEP; $2.5^\circ \times 2.5^\circ$ spatial resolution), and ERA5. An additional South Sandwich Islands case is shown in Extended Data Fig. 2 as well as in Supplementary Figure 2 (Supplementary Text 1.1), where large deviations are evident. All three meteorological products broadly predict the correct wind direction across different PBL TKE parameterizations, but the predicted particle distribution does not always match hand-logged track positions, especially beyond a couple hundred kilometers.

To estimate HYSPLIT position error, we sum the minimum distance from each hand-logged track point T_n to the nearest HYSPLIT point H_k. This is given by

$$e = \sum_n min\{\sum_k \sqrt{(T_n - H_k)^2}\} \tag{1}$$

where e is the error in km. Applied to all hand-logged tracks, this metric gives an average nearest-neighbor distance of ∼20 km for ERA5 and ∼50 km for NCEP (Extended Data Fig. 3a). ERA5 performs best, likely because of its higher spatial resolution and assimilation of cloud-top motion winds retrieved by geostationary satellites[28].

Although plume position is fairly well modeled with HYSPLIT and ERA5 reanalysis meteorology, plume width can vary significantly depending on atmospheric stability, wind speed, choice of turbulence scheme, and mixing methods. To examine the effect of varying the mixing scheme, we test the following HYSPLIT options:

1. Flux-based PBL stability, horizontal turbulence proportional to vertical turbulence, and height-varying vertical mixing.

2. Deformation-based horizontal turbulence, U/T-based PBL stability, and PBL-averaged vertical mixing.

3. As in 2, but with height-varying vertical mixing.

Different mixing schemes have little effect on plume location but strongly affect plume width (Extended Data Fig. 2, 3b). Plumes are widest when horizontal turbulence scales with vertical turbulence and narrowest when based on velocity deformation. The

deformation-based, height-varying PBL schemes best matches observed track widths, although all schemes widen plumes too rapidly with distance, suggesting that HYSPLIT overestimates marine-PBL dispersion.

Aerosol Radiative Forcing The aerosol indirect radiative effect is computed following Christensen et al. (2022)[3]:

$$RE_{aci} = -F^{\downarrow}\phi_{atm}\frac{f_c\alpha_c(1-\alpha_c)}{3N_d}\left(1+\frac{5}{2}\frac{\Delta\ln L}{\Delta\ln N_d}+\frac{3(\alpha_c-\alpha_{clr})}{\alpha_c(1-\alpha_c)}\frac{\Delta\ln f_c}{\Delta\ln N_d}\right)\Delta N_d \quad (2)$$

where $F^{\downarrow}$ is the annual mean incoming solar radiative flux at the top of the atmosphere with a value of 340.2 W m^{-2} (at each site), ϕ_{atm} is the transfer function accounting for the average albedo of the air above the surface and clouds (average value 0.7), f_c is low-level cloud fraction, α_c is cloud albedo, α_{clr} is clear-sky albedo, N_d is cloud droplet number concentration, L is liquid water path, and ΔN_d is the change in cloud droplet number concentration between CAM6 simulation experiments (plume – baseline and plume-noSO_2 – baseline). RE_{aci} is similarly computed from satellite observations using the same incoming solar flux and clear-sky albedos for each location. Cloud albedo is calculated from cloud optical thickness using the Eddington approximation for a nonabsorbing medium, $\alpha_c = \frac{(1-g)\tau_c}{2+(1-g)\tau_c}$, with assymetry parameter, g, $\sim$0.85 for warm clouds[24]. Changes in cloud properties are determined by comparing polluted tracks with their controls.

General Circulation Modeling CAM6 (Community Atmosphere Model version 6) is an atmospheric GCM with double-moment bulk cloud microphysics and chemistry schemes[29,30]. The model includes comprehensive aerosol–cloud interactions[29], including cloud activation and aerosol scavenging[31], through the four-mode Modal Aerosol Model (MAM4)[32] coupled to sulfate chemistry[33]. New particle formation (NPF) in CAM6/MAM4 is represented using sulfuric-acid nucleation pathways, including binary H_2SO_4–H_2O nucleation[34] and a boundary-layer activation-type/ion-mediated pathway, as described by Liu et al. (2012, 2016)[33,32]. H_2SO_4 vapor is produced by gas-phase SO_2 oxidation and condenses onto pre-existing aerosol. Oxidant fields are prescribed rather than prognosed; they come from an external climatology, vary in space and time (e.g., monthly with diurnal scaling)[33,29], and are applied identically in the baseline, plume, and plume-noSO_2 runs. The climatology is derived from a CAM6-MAM simulation with fully prognostic chemical fields.

Aerosols are represented by fixed log-normal modes, with sulfate residing mainly in the accumulation mode (representative diameter $\simeq$ 0.16 μm, geometric standard deviation $\simeq$ 1.8) and Aitken mode ($\simeq$ 0.034μm, $\sigma \simeq$ 1.6), and a smaller contribution in the coarse mode ($\simeq$ 2.23μm, $\sigma \simeq$ 1.8)); representative diameters are estimated from the 10th–90th percentile ranges reported in Liu et al. (2012, Table 1). Transported gas species include SO_2, H_2O_2, dimethyl sulphide (DMS), H_2SO_4, and a lumped semi-volatile organic species. H_2SO_4 vapor is produced by gas-phase SO_2 oxidation and is lost mainly by condensation

onto pre-existing aerosol and, to a lesser extent, by aqueous uptake in cloud water (about 4%)[33]. Aqueous oxidation of SO_2 to sulfate by H_2O_2 and O_3 in cloud water is also included and is a major production pathway that adds sulfate mass to existing aerosol modes. CAM6 further includes in-cloud and below-cloud scavenging, so interstitial non-activated particles, including newly nucleated and small Aitken-mode particles, may be collected by cloud droplets and precipitation, damping the net contribution of nucleation and condensational growth to CCN concentration[32].

Primary sulfate does not have a unique size distribution, but instead inherits the modal parameters of its host mode. CCN attributed to the prescribed 2.5% primary sulfate largely represent sub-grid sulfate production, which is sensitive to environmental conditions[35,36], especially in remote oceanic regions with low background aerosol loading. The substantial radiative effect retained in the plume-noSO2 experiment does not fully isolate only the volcanic 2.5% primary sulfate term, because background sulfur sources such as DMS remain active. MAM4 also treats particulate organic matter, dust, sea salt, and black carbon aerosols. Cloud properties simulated using the Cloud Feedback Model Intercomparison Project Observational Simulator Package (COSP) are utilized for quantifying RE_{aci}. The lack of negative simulated LWP responses in CAM6 (Fig. 6) is common in GCMs[1] and is probably due to an insufficient connection between cloud-top entrainment and cloud droplet sedimentation rates that are affected by increased N_d in boundary layer clouds[37]. Together, these parameterizations enable CAM6 to simulate the gas, aerosol, and cloud interactions needed to assess aerosol radiative forcing.

The CAM6 simulations use an approximately $1.25^\circ \times 1^\circ$ longitude-latitude grid with 32 vertical levels from the surface to the model top. CAM6 is nudged with the Modern-Era Retrospective Analysis for Research and Applications, version 2 (MERRA-2), reanalysis[38]. Three simulation types are carried out: 1) a control (**baseline**) simulation using all anthropogenic and natural aerosol sources from 2010 excluding shipping, volcanic, and industrial sources as described in Eyring et al. (2016)[39], 2) a **plume+baseline** run, identical to the baseline but with emissions prescribed at the selected regions listed in Extended Data Table 1 mostly based on Carn et al.[40] observations, and 3) a **plume-noSO_2** run, identical to plume+baseline but without added SO_2.

The radiative effect estimated from the CAM6 plume–baseline difference includes contributions from both ACI and aerosol direct radiative effects. Although our experimental design does not explicitly separate these terms, previous observational analyses of volcanic plumes suggest that the direct aerosol effect can constitute a substantial fraction of the total forcing. For example, Chen et al. (2024)[41] estimate that roughly half of the observed radiative effect during the 2008 and 2018 Kīlauea eruptions arose from aerosol direct effects, with cloud fraction adjustments contributing strongly to the ACI component. In contrast, CAM6 simulates a negligible cloud fraction adjustment, indicating that the modeled radiative response is dominated by microphysical rather than macrophysical cloud changes. This discrepancy likely reflects known limitations in models' ability to capture cloud fraction sensitivity to aerosol perturbations and mesoscale dynamics, and

highlights the need for further development and evaluation of cloud adjustment processes using coordinated model–observation frameworks.

Particle-resolved aerosol modeling The Particle Monte Carlo Model for Simulating Aerosol Interactions and Chemistry (PartMC-MOSAIC)[42,8] is a detailed aerosol model that tracks the size and composition of thousands of individual particles within a Lagrangian air parcel. The particle population evolves through chemical and physical processes, including NPF, gas condensation and evaporation, coagulation, mixing with background air, and deposition. We initialize PartMC-MOSAIC with SO_2 emissions and primary particles representative of the conditions near the Halema‘uma‘u Crater vent[18]. We track particle evolution during transport away from the vent; therefore, no additional particle or gas emissions are included, although the parcel dilutes with the background air. During transport, SO_2 oxidizes to form H_2SO_4 through MOSAIC chemistry with temperature-dependent rate constants[8]. The resulting H_2SO_4 partitions to the particle phase through NPF and condensation onto pre-existing aerosol, computed with size- and composition-dependent Fuchs–Sutugin mass transfer including the Kelvin effect when vapor supersaturation permits. NPF is represented using PartMC's built-in sulfuric acid nucleation scheme following Kuang et al. (2008)[43], in which the nucleation rate is given by $J = K_{\mathrm{NPF}}[H_2SO_4]^2$. Here, J is the nucleation rate, K_{NPF} is an empirical nucleation-rate coefficient set to 10^{-18} m^3 s^{-1}, and $[H_2SO_4]$ denotes the gas-phase sulfuric acid number concentration. Newly formed particles are initialized as sulfate particles with diameter $D_{\mathrm{NPF}} = 1$ nm. This PartMC-MOSAIC parameterization is distinct from the binary H_2SO_4–H_2O nucleation scheme used in CAM6 and does not include explicit temperature or relative-humidity dependence in the nucleation-rate expression. Ternary or base-enhanced pathways involving NH_3 or amines, as well as ion-mediated enhancements, are not explicitly represented in these PartMC-MOSAIC sensitivity experiments. This choice reflects the expectation that basic vapors are limited in the remote marine PBL near Kīlauea. If present, NH_3, amines, or ions could increase particle production, although the effect on CCN would depend on subsequent growth by condensation and coagulation relative to dilution and removal. The particle population is further modified by Brownian coagulation, which merges newly formed sulfate particles and accelerates growth into CCN-relevant sizes over downstream timescales. Photolysis-dependent gas-phase chemistry produces a diurnally varying oxidizing capacity: daytime OH production promotes SO_2 oxidation and H_2SO_4 formation, whereas nighttime H_2SO_4 production and nucleation are strongly reduced. Temperature, pressure, relative humidity, background gas and aerosol concentrations, and mixing-layer conditions are prescribed through the PartMC scenario inputs, and the parcel mixes with background air at a fixed dilution rate of 5×10^{-6} s^{-1}. These prescribed fields affect SO_2 oxidation, H_2SO_4 production, condensation, and gas–particle partitioning, but the PartMC nucleation-rate expression itself does not include an explicit temperature or relative-humidity dependence.

Our box-model experiments represent clear-air plume segments and therefore exclude in-cloud aqueous SO_2 oxidation. In clouds, SO_2 dissolves into cloud droplets and is ox-

idized in the aqueous phase to sulfate. After droplet evaporation, this sulfate remains primarily as added mass on activated-particle residuals, modifying their size, composition, and hygroscopicity rather than directly producing fresh nanometer-scale particles through gas-phase nucleation[44]. Thus, cloud processing redistributes sulfur into the cloud-processed aerosol population and can reduce the SO_2 available for subsequent clear-air OH oxidation to H_2SO_4. In our framework, these competing pathways are represented in CAM6/MAM4, which includes gas- and aqueous-phase sulfate production, nucleation and growth, coagulation, cloud processing, and wet scavenging within a modal aerosol modeling framework. The PartMC-MOSAIC box-model simulations are used to isolate gas-phase nucleation, condensation, and coagulation pathways, while explicit in-cloud aqueous chemistry is left for future work.

To isolate the effects of individual aerosol processes on CCN concentration, we run each scenario in three configurations: all processes described above included, no NPF, and no coagulation, labeled "all on," "no NPF," and "no coagulation," respectively, in Extended Data Fig. 8. The simulation settings, model code details, and input files are available from Zenodo (`https://doi.org/10.5281/zenodo.20041770`[45]).

Data availability

MODIS Collection 6 products are available at `https://earthdata.nasa.gov`. ECMWF data were obtained from `https://www.ecmwf.int`. Hand-logged positions of pollution tracks in satellite imagery and input parameters for PartMC-MOSAIC are available from Zenodo (https://doi.org/10.5281/zenodo.20041770, Christensen, 2024)[45].

Code availability

HYSPLIT trajectory code is available at `https://www.ready.noaa.gov/HYSPLIT.php`. The release version of CAM6 in the Community Earth System Model Version 2 is available via `https://www.cesm.ucar.edu/models/cesm2`[30]. PartMC is available via `https://github.com/compdyn/partmc`. PartMC version 2.6.1 was used for this study. The MOSAIC model is available via `https://github.com/pnnl/MOSAIC/`. All public data and code availability websites were last accessed on 7 June 2024.

References

[23] V. E. Fioletov, C. A. McLinden, D. Griffin, I. Abboud, N. Krotkov, P. J. T. Leonard, C. Li, J. Joiner, N. Theys, and S. Carn. Version 2 of the global catalogue of large anthropogenic and volcanic so2 sources and emissions derived from satellite measurements. *Earth System Science Data*, 15(1):75–93, 2023. ISSN 1866-3508. doi: 10.5194/essd-15-75-2023. URL `<GotoISI>://WOS:000907575600001`.

[24] J.-L. Brenguier, H. Pawlowska, L. Schuller, R. Preusker, J. Fischer, and Y. Fouquart.

Radiative properties of boundary layer clouds: Droplet effective radius versus number concentration. *Journal of the Atmospheric Sciences*, 57(6):803–821, 2000. doi: 10.1175/1520-0469(2000)057<0803:RPOBLC>2.0.CO;2. URL https://doi.org/10.1175/1520-0469(2000)057<0803:RPOBLC>2.0.CO;2.

[25] D. P. Grosvenor, O. Sourdeval, P. Zuidema, A. Ackerman, M. D. Alexandrov, R. Bennartz, R. Boers, B. Cairns, J. C. Chiu, M. Christensen, H. Deneke, M. Diamond, G. Feingold, A. Fridlind, A. Hunerbein, C. Knist, P. Kollias, A. Marshak, D. McCoy, D. Merk, D. Painemal, J. Rausch, D. Rosenfeld, H. Russchenberg, P. Seifert, K. Sinclair, P. Stier, B. van Diedenhoven, M. Wendisch, F. Werner, R. Wood, Z. Zhang, and J. Quaas. Remote sensing of droplet number concentration in warm clouds: A review of the current state of knowledge and perspectives. *Reviews of Geophysics*, 56(2):409–453, 2018. doi: 10.1029/2017RG000593. URL https://agupubs.onlinelibrary.wiley.com/doi/abs/10.1029/2017RG000593.

[26] M. S. Segrin, J. A. Coakley Jr., and W. R. Tahnk. Modis observations of ship tracks in summertime stratus off the west coast of the united states. *Journal of the Atmospheric Sciences*, 64:4330–4345, 2007. doi:10.1175/2007JAS2308.1.

[27] R. Draxler and G. Hess. An overview of the hysplit 4 modeling system for trajectories, dispersion, and deposition. *Australian Meteorological Magazine*, 47:295–308, 12 1998.

[28] H. Hersbach, B. Bell, P. Berrisford, S. Hirahara, A. Horányi, J. Muñoz-Sabater, J. Nicolas, C. Peubey, R. Radu, D. Schepers, A. Simmons, C. Soci, S. Abdalla, X. Abellan, G. Balsamo, P. Bechtold, G. Biavati, J. Bidlot, M. Bonavita, G. De Chiara, P. Dahlgren, D. Dee, M. Diamantakis, R. Dragani, J. Flemming, R. Forbes, M. Fuentes, A. Geer, L. Haimberger, S. Healy, R. J. Hogan, E. Hólm, M. Janisková, S. Keeley, P. Laloyaux, P. Lopez, C. Lupu, G. Radnoti, P. de Rosnay, I. Rozum, F. Vamborg, S. Villaume, and J.-N. Thépaut. The era5 global reanalysis. *QJRMS*, 146(730):1999–2049, 2020. doi: 10.1002/qj.3803.

[29] A. Gettelman, H. Morrison, S. Santos, P. Bogenschutz, and P. M. Caldwell. Advanced Two-Moment Bulk Microphysics for Global Models. Part II: Global Model Solutions and Aerosol–Cloud Interactions. *J. Climate*, 28(3):1288–1307, 2015. ISSN 0894-8755. doi: 10.1175/JCLI-D-14-00103.1.

[30] G. Danabasoglu, J.-F. Lamarque, J. Bacmeister, D. A. Bailey, A. K. DuVivier, J. Edwards, L. K. Emmons, J. Fasullo, R. Garcia, A. Gettelman, C. Hannay, M. M. Holland, W. G. Large, P. H. Lauritzen, D. M. Lawrence, J. T. M. Lenaerts, K. Lindsay, W. H. Lipscomb, M. J. Mills, R. Neale, K. W. Oleson, B. Otto-Bliesner, A. S. Phillips, W. Sacks, S. Tilmes, L. van Kampenhout, M. Vertenstein, A. Bertini, J. Dennis, C. Deser, C. Fischer, B. Fox-Kemper, J. E. Kay, D. Kinnison, P. J. Kushner, V. E. Larson, M. C. Long, S. Mickelson, J. K. Moore, E. Nienhouse, L. Polvani, P. J. Rasch, and W. G. Strand. The Community Earth System Model Version 2 (CESM2).

Journal of Advances in Modeling Earth Systems, 12(2):e2019MS001916, 2020. ISSN 1942-2466. doi: 10.1029/2019MS001916.

[31] H. Abdul-Razzak and S. J. Ghan. A parameterization of aerosol activation 2. Multiple aerosol types. *J. Geophys. Res*, 105(D5):6837–6844, 2000.

[32] X. Liu, P.-L. Ma, H. Wang, S. Tilmes, B. Singh, R. C. Easter, S. J. Ghan, and P. J. Rasch. Description and evaluation of a new four-mode version of the Modal Aerosol Module (MAM4) within version 5.3 of the Community Atmosphere Model. *Geoscientific Model Development*, 9(2):505–522, Feb. 2016. ISSN 1991-959X. doi: 10.5194/gmd-9-505-2016.

[33] X. Liu, R. C. Easter, S. J. Ghan, R. Zaveri, P. Rasch, X. Shi, J.-F. Lamarque, A. Gettelman, H. Morrison, F. Vitt, A. Conley, S. Park, R. Neale, C. Hannay, A. M. L. Ekman, P. Hess, N. Mahowald, W. Collins, M. J. Iacono, C. S. Bretherton, M. G. Flanner, and D. Mitchell. Toward a minimal representation of aerosols in climate models: description and evaluation in the community atmosphere model cam5. *Geoscientific Model Development*, 5(3):709–739, 2012. doi: 10.5194/gmd-5-709-2012. URL `https://gmd.copernicus.org/articles/5/709/2012/`.

[34] H. Vehkamäki, M. Kulmala, I. Napari, K. E. J. Lehtinen, C. Timmreck, M. Noppel, and A. Laaksonen. An improved parameterization for sulfuric acid–water nucleation rates for tropospheric and stratospheric conditions. *Journal of Geophysical Research: Atmospheres*, 107(D22):4622, 2002. doi: 10.1029/2002JD002184.

[35] F. Yu. Diurnal and seasonal variations of ultrafine particle formation in anthropogenic so_2 plumes. *Environmental Science & Technology*, 44(6):2011–2015, 2010. doi: 10.1021/es903228a.

[36] R. G. Stevens and J. R. Pierce. The contribution of plume-scale nucleation to global and regional aerosol and ccn concentrations: evaluation and sensitivity to emissions changes. *Atmospheric Chemistry and Physics*, 14(24):13661–13679, 2014. doi: 10.5194/acp-14-13661-2014. URL `https://acp.copernicus.org/articles/14/13661/2014/`.

[37] C. S. Bretherton, P. N. Blossey, and J. Uchida. Cloud droplet sedimentation, entrainment efficiency, and subtropical stratocumulus albedo. *Geophysical Research Letters*, 34(3), 2007. ISSN 0094-8276. doi: 10.1029/2006gl027648.

[38] A. Molod, L. Takacs, M. Suarez, and J. Bacmeister. Development of the GEOS-5 atmospheric general circulation model: Evolution from MERRA to MERRA2. *Geosci. Model Dev.*, 8(5):1339–1356, May 2015. ISSN 1991-9603. doi: 10.5194/gmd-8-1339-2015.

[39] V. Eyring, S. Bony, G. A. Meehl, C. A. Senior, B. Stevens, R. J. Stouffer, and K. E. Taylor. Overview of the Coupled Model Intercomparison Project Phase 6 (CMIP6)

experimental design and organization. *Geosci. Model Dev.*, 9(5):1937–1958, May 2016. ISSN 1991-9603. doi: 10.5194/gmd-9-1937-2016.

[40] S. Carn, V. Fioletov, C. McLinden, C. Li, and N. Krotkov. A decade of global volcanic so2 emissions measured from space. *Scientific Reports*, 7:1899–1905, 2017. doi: https://doi.org/10.1038/srep44095.

[41] Y. Chen, J. Haywood, Y. Wang, F. Malavelle, G. Jordan, A. Peace, D. G. Partridge, N. Cho, L. Oreopoulos, D. Grosvenor, P. Field, R. P. Allan, and U. Lohmann. Substantial cooling effect from aerosol-induced increase in tropical marine cloud cover. *Nature Geoscience*, 17:404–410, 2024. doi: 10.1038/s41561-024-01427-z.

[42] N. Riemer, M. West, R. A. Zaveri, and R. C. Easter. Simulating the evolution of soot mixing state with a particle-resolved aerosol model. *Journal of Geophysical Research: Atmospheres*, 114(D9), 2009.

[43] C. Kuang, P. H. McMurry, A. V. McCormick, and F. L. Eisele. Dependence of nucleation rates on sulfuric acid vapor concentration in diverse atmospheric locations. *Journal of Geophysical Research: Atmospheres*, 113(D10):D10209, 2008. doi: 10.1029/2007JD009253.

[44] J. H. Seinfeld and S. N. Pandis. *Atmospheric Chemistry and Physics: From Air Pollution to Climate Change*. John Wiley & Sons, Hoboken, NJ, 3rd edition, 2016. ISBN 978-1-118-94740-1. See sections on aqueous-phase oxidation of SO_2 in cloud water (cloud/multiphase chemistry chapters).

[45] M. Christensen. Pollution tracks in lagrangian framework dataset, June 2024. URL `https://doi.org/10.5281/zenodo.20041770`.